

Magnetic phase transition induced ferroelectric polarization in BaFeF₄ with room-temperature weak ferromagnetism

Fan Zhang,¹ Yongsen Tang,² Ranran Li,¹ Tianyu Liu,² Dingshi Xu,¹ Yinzhu Chen,¹ Ben Niu,² Shijun Yuan,¹ Sai Qin,³ Zhibo Yan,² Jun Du,^{2,*} Di Wu,² Qi Li,^{1,2} Shuai Dong,^{1,†} and Qingyu Xu^{1,2,‡}

¹*School of Physics, Southeast University, Nanjing 211189, China*

²*National Laboratory of Solid State Microstructures, Nanjing University, Nanjing 210093, China*

³*School of Sciences, Changzhou Institute of Technology, Changzhou 213032, China*



(Received 13 December 2021; accepted 31 March 2022; published 20 April 2022)

The BaMF₄ ($M = \text{Fe, Co, Ni, and Mn}$) family consists of typical multiferroic materials, having antiferromagnetism at around liquid nitrogen temperature. In this paper, polycrystalline BaFeF₄ has been prepared by solid state reaction. The slight deficiency of Fe leads to the coexistence of valence states of + 2 and + 3, facilitating the electrons to hop between the neighboring Fe²⁺ and Fe³⁺ ions through the middle F⁻ ion, leading to the strong double exchange interaction with weak ferromagnetism above room temperature. A bifurcation at ~ 170 K between the zero-field-cooled and field-cooled temperature-dependent magnetization curves indicates the onset of two-dimensional antiferromagnetism, which is completed at ~ 125 K with the sudden drop of magnetization. Despite being a type-I multiferroic, its magnetoelectricity (ME) can be evidenced by the pyroelectric current, which shows a peak starting at ~ 170 K and finishing at ~ 125 K. The saturated ferroelectric polarization change of $\sim 34 \mu\text{C}/\text{m}^2$ is observed, which is switchable by the reversed poling electric field, and decreases to $\sim 30 \mu\text{C}/\text{m}^2$ under a magnetic field of 90 kOe. This ME can be qualitatively reproduced by first-principles calculations. Our results represent substantial progress to search for high-temperature multiferroics in ferroelectric fluorides.

DOI: [10.1103/PhysRevMaterials.6.044408](https://doi.org/10.1103/PhysRevMaterials.6.044408)

I. INTRODUCTION

Multiferroic materials, possessing ferroelectric and magnetic orderings simultaneously, provide fascinating functions of mutual control of ferroelectricity and magnetism by electric and magnetic fields through magnetoelectric (ME) coupling [1–3]. However, single-phase multiferroic materials are very rare since most studies are focused on oxide perovskite ferroelectric materials containing 3d transition metal (TM) ions [4–7]. Due to covalent bonding between O and 3d TM ions, the requirements for the outer shell electronic structure for 3d TM ions are contradictory for ferroelectricity and ferromagnetism, ferrimagnetism, or antiferromagnetism [8]. To break this limit, one possible solution is to search for single-phase multiferroic materials with more ionic bonding containing 3d TM ions [9].

The BaMF₄ ($M = \text{Fe, Co, Ni, and Mn}$) family consists of typical ferroelectric materials, which was reported by Eibschütz and Guggenheim [10] and Eibschütz *et al.* [11]. Ferroelectricity with spontaneous polarization of several $\mu\text{C}/\text{cm}^2$ has been reported by pyroelectric measurements, and the Curie temperature was determined to be much higher than room temperature [11–13]. However, the superexchange interaction between the neighboring 3d TM ions through the

middle F⁻ ions generally leads to antiferromagnetic coupling. Furthermore, due to the ionic bonding between 3d TM and F⁻ ions, the overlapping of the electron clouds is rather small, leading to the much weaker exchange interaction. Thus, the magnetic structure of BaMF₄ is essentially antiferromagnetic, with Néel temperature T_N much lower than room temperature (20–80 K) [14].

ME in BaMF₄ has been preliminarily studied. Weak ferromagnetism has been observed in BaMnF₄, which has been attributed to ferroelectrically induced spin canting between the neighboring Mn²⁺ ions through the ME effect [15]. Magnetization in BaMnF₄ has the dominant orientation after field cooling due to coupling with spontaneous polarization through ME, and the exchange bias effect has been observed [16]. Ederer and Spaldin [14] have calculated the magnetic structure of BaNiF₄, and spin canting between the neighboring Ni²⁺ ions has been reported, which leads to the net magnetic moment. However, due to the symmetry being forbidden, the net magnetic moments were aligned antiparallel to each other to form weak antiferromagnetism. They predicted the electric-field-switchable magnetic order parameter due to its orientation depending on spontaneous polarization. Weak antiferromagnetism in BaNiF₄ has been demonstrated by wasp-waisted field-dependent magnetization hysteresis loops [17]. However, direct observation of the ME effect has not yet been reported.

Motivated by these discussions, it is necessary to realize ferromagnetism above room temperature in BaMF₄ materials, and the dependence of the ME effect on electric polarization

*jdu@nju.edu.cn

†sdong@seu.edu.cn

‡xuqingyu@seu.edu.cn

should be directly measured. In this paper, BaFeF_4 has been investigated since Fe is a typical $3d$ TM element which always forms a ferromagnetic compound with high Curie temperature. By slight deviation from the stoichiometric BaFeF_4 with less Fe concentration, a portion of the Fe ions change to be in $+3$ valence state. Thus, a double exchange interaction between the neighboring Fe^{2+} and Fe^{3+} ions can be formed, leading to ferromagnetic exchange interaction and weak ferromagnetism above room temperature. Furthermore, the electric field reversible polarization change and magnetic field tunable polarization change are observed, which are ascribed to the phase transition to two-dimensional antiferromagnetism.

II. EXPERIMENTAL DETAILS

BaFeF_4 is synthesized by solid state reaction. The molar ratio of BaF_2 and FeF_2 powders is finely adjusted to be 1:0.95 to obtain a pure phase sample. The raw materials are mixed and ground for 1 h in a mortar. The mixture is pressed into small discs with diameters of 10 mm, which are then put into a copper tube. The tubes are sealed in an arc-melting furnace filled with pure Ar atmosphere (99.99%). Finally, the copper tubes are placed in a furnace and heated at the temperature of 650°C for 36 h. After that, the furnace is naturally cooled down to room temperature, and the final products are obtained.

The crystal structure is studied by x-ray diffraction (XRD, Rigaku Smartlab 3) with Cu $K\alpha$ radiation ($\lambda = 1.5406 \text{ \AA}$). The surface morphology is characterized by a scanning electron microscope (SEM, FEI Inspect F50), and the elemental composition is analyzed by the attached energy-dispersive x-ray spectroscope (EDS). The valence state of each element is analyzed by x-ray photoelectron spectroscopy (XPS, PREVAC) with an Al $K\alpha$ x-ray source ($h\nu = 1486.6 \text{ eV}$). Second-harmonic generation (SHG) measurements are carried out on a home-built system. The wavelength of the excitation laser is 800 nm, which is frequency doubled by a barium borate crystal from a femtosecond laser (Chameleon Compact OPO, center wavelength: 900 nm, repetition rate: 80 MHz), and the integration time is 1s. The excitation laser is focused by a microscopy objective (50 \times , numerical aperture: 0.5). The ferroelectric properties are tested by a scanning probe microscope (SPM, Asylum Research Cypher). The magnetic properties are studied by a superconducting quantum interference device (Quantum Design). The T dependence of the pyroelectric current (I_{py}) is collected upon T increasing from 5 to 300 K using a Keithley 6514 programmable electrometer, with a sample warming rate of 4 K/min. In addition, to explore ME coupling, the measurement is performed in a physical property measurement system (Quantum Design) under a magnetic field of 90 kOe. The variation in electric polarization (ΔP) is obtained by integrating the pyroelectric current with the time. To confirm the electric field reversible ΔP , an electric field of $\pm 2 \text{ kV/cm}$ is applied during the cooling process to 5 K, which is removed during the warming process for the pyroelectric current measurements.

Our density functional theory (DFT) calculations are performed using the Vienna *Ab initio* Simulation Package [18]. The electronic interactions are described by projector-augmented-wave pseudopotentials with semicore

states treated as valence states [19]. To precisely describe the crystal structure, the generalized gradient approximation with Perdew-Burke-Ernzerhof functional modified for solids (PBEsol) parametrization is adopted [20]. To count the correlation effect, the Hubbard $U_{\text{eff}} = U - J = 4 \text{ eV}$ [21] is applied to Fe $3d$ orbitals using the Dudarev approach [22]. The plane-wave cutoff energy is fixed as 500 eV. The k-point grids of $5 \times 3 \times 6$ are adopted for both structural relaxation and static computation. The convergent criterion for the energy was set to 10^{-6} eV , and that of the Hellman-Feynman forces during the structural relaxation is 0.001 eV/\AA . The polarization is calculated using the standard Berry phase method [23,24].

III. RESULTS AND DISCUSSION

A. Crystal structure, micromorphology, and elemental analysis

It has been reported that the crystal structure of BaMF_4 is orthorhombic with a $[MF_6]$ octahedral chain, and the space group is $A2_1am$ [25,26]. The crystal structure of BaFeF_4 powders is studied by XRD, and the pattern is shown in Fig. 1(a). The Rietveld refinement is applied to get the crystal lattice constants by GSAS-II using the crystallographic data of BaFeF_4 (CIF ID#1539611) [27]. The discrepancy factors of refinement are $W_{\text{Rp}} = 9.31\%$ and $\chi^2 = 3.119$. The pure phase is confirmed by the fact that all the peaks can be indexed to the standard data of BaFeF_4 . The refined results show the orthorhombic structure for the cell with parameters of $a = 5.7680(6) \text{ \AA}$, $b = 14.9640(8) \text{ \AA}$, and $c = 4.2592(7) \text{ \AA}$, and the cell volume is $V = 366.634 \text{ \AA}^3$. The schematic crystal structure is shown in the inset of Fig. 1(a), in that the $[\text{FeF}_6]$ octahedra form the linear chain along the c axis and the puckered sheet along the a axis, and Ba cations are separated by these octahedrons, which agrees well with previous reported data [21,28].

The SEM image of BaFeF_4 powders [Fig. 1(b)] shows the irregular shape with different sizes. The elemental mappings for Ba, Fe, and F are shown in the inset, and the uniform color indicates homogeneous distribution. According to the EDS results, the atomic ratio of Fe and Ba is ~ 0.89 , indicating slight deficiency of Fe in BaFeF_4 powders, which is due to slightly smaller amount of FeF_2 than the stoichiometric composition. Thus, to balance the valence state of each element, the valence state of Fe should deviate from $+2$ and partly in $+3$, which will be confirmed by the following XPS results.

XPS measurements are performed to study the valence state of each element, and the collected spectra are shown in Fig. 2. As can be seen, the survey spectrum [Fig. 2(a)] shows the presence of Ba, C, O, F, and Fe elements in the BaFeF_4 powder. Additionally, there are Auger signals assigned to the Fe KMM and F KLL transitions. C and O may come from the adsorbed impurities in the air, and C $1s$ at 284.6 eV is used to correct the instrument error. Ba $3d_{3/2}$ and $3d_{5/2}$ are at 794.9 eV and 779.8 eV, respectively, leading to the separation of 15.1 eV, which can be attributed to Ba^{2+} ions [29,30]. The high-resolution Fe $2p$ spectrum is shown in Fig. 2(c). The spectrum is deconvoluted into the main peaks from Fe^{2+} and Fe^{3+} together with the corresponding satellite peaks. As can be seen, the fitted curve agrees with the experimental curve quite well. The peaks at 710.7 and 724.3 eV are from

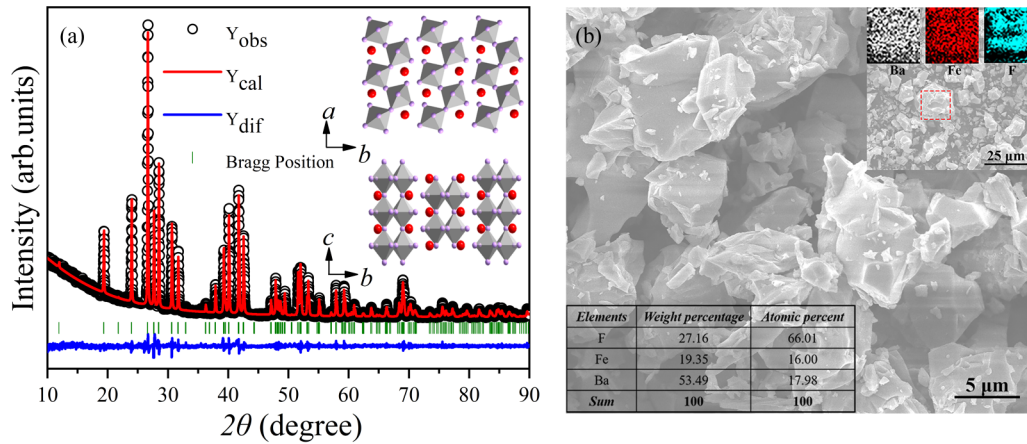


FIG. 1. (a) Rietveld refined x-ray diffraction (XRD) pattern of the BaFeF₄ powders; the inset shows the schematic diagram of the crystal structure viewed along [001] and [100] orientations. (b) The scanning electron microscope (SEM) image of BaFeF₄ powders; the insets show the elemental (Ba, Fe, and F) mapping (top right) from the selected area marked by the red dotted box; and the energy-dispersive x-ray spectroscopy (EDS) results of the concentration of each element.

Fe²⁺, like those of FeF₂ [31]. The peaks at 712.4 and 726 eV confirm the existence of Fe³⁺ ions due to the nonstoichiometric raw materials with less FeF₂ [32]. However, the concentration of Fe³⁺ should be low due to the much smaller peak area. A rough estimation of Fe³⁺ concentration can be calculated to be ~33% from the area ratio with Fe²⁺ of 1:2, if we assume the equal scattering factor of Fe²⁺ and Fe³⁺ ions. This is quite consistent with the EDS result of 11%

Fe deficiency, which will make 25% Fe in the +3 valence state if the F concentration keeps constant. The XPS peak of F 1s can be deconvoluted to two peaks. The peak at 684.9 eV can be ascribed to Fe-F bonding in the stoichiometric area [33]. The other peak at 684.2 eV can be attributed to Fe-F bonding in the Fe deficient area. The area ratio of the F 1s peak at 684.2 eV to that at 684.9 eV is also 1:2, which is consistent with the area ratio of Fe³⁺ to Fe²⁺.

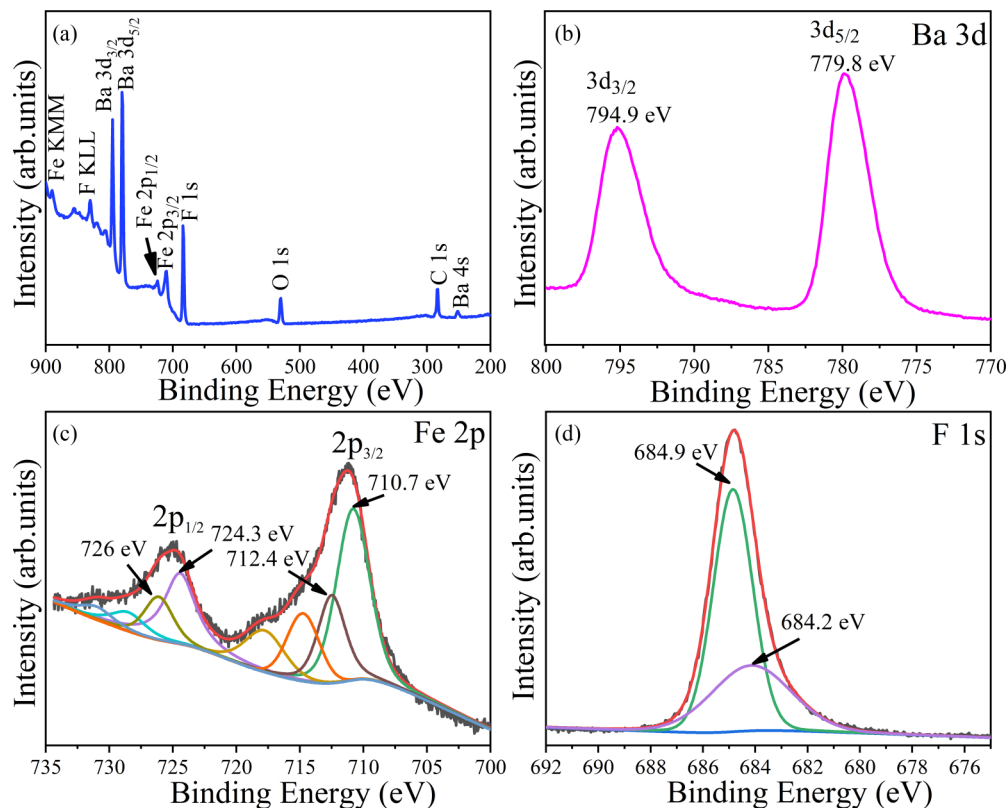


FIG. 2. (a) The full-scan spectra, (b) Ba 3d, (c) Fe 2p, and (d) F 1s x-ray photoelectron spectroscopy (XPS) spectra of BaFeF₄ powders.

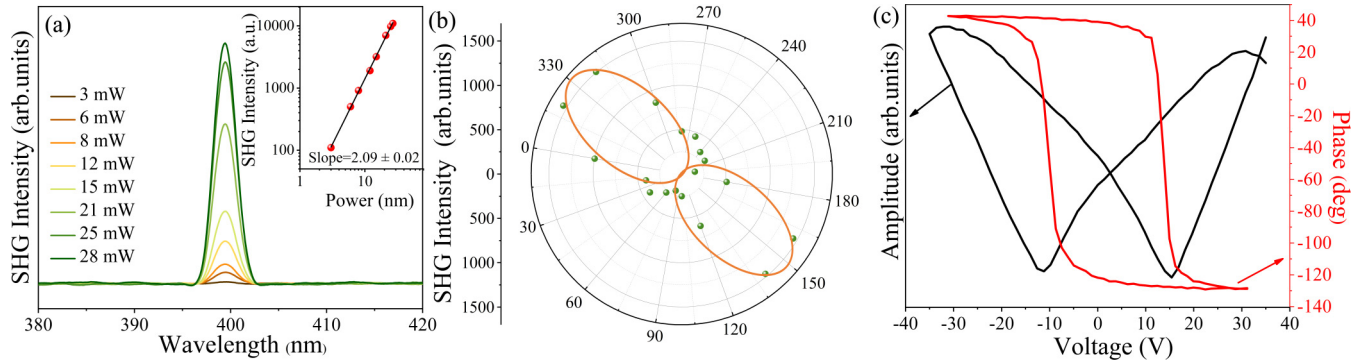


FIG. 3. Second-harmonic generation (SHG) results are measured at the room temperature. (a) SHG intensity of BaFeF₄ with different excitation power; the inset is the excitation power-dependent SHG intensity in logarithmic coordinates. (b) Polarization angle dependence of the SHG intensity. (c) Phase-voltage and amplitude-voltage piezoelectric curves at room temperature.

B. Nonlinear optical behavior, magnetic phase transitions, and ferroelectric polarization

The spontaneous polarization of BaFeF₄ has been confirmed by the pyroelectric current measurement, but the reverse of polarization by electric field has not yet been reported, which has been ascribed to the much larger radius of Fe²⁺ ions, leading to the too-high energy barrier [21]. BaFeF₄ has a polar space group, which can be demonstrated by SHG measurements. The excitation wavelength is 800 nm, and the corresponding SHG signal appears at 400 nm. The SHG intensity increases with the enhancement of power, as shown in Fig. 3(a). The inset of Fig. 3(a) shows the SHG intensity dependence on the power intensity, both in log scale, and the linear fitting shows the slope of ~ 2.09 , which is very close to the theoretical value of 2 [34]. This indicates that SHG intensity is proportional to the square of the power intensity, demonstrating the nonlinear optical principal [35,36]. Since the polarization-resolved SHG shows crystal-symmetry dependence, we perform angle-dependent SHG intensity measurements with the excitation laser parallel to polarization. The polarization-dependent SHG intensity in Fig. 3(b) shows a twofold rotational symmetry by varying the azimuthal angle θ , with its minimum at 60° and maximum at 150°, which also exhibits nonlinear behavior.

We perform electric-field-dependent polarization $P(E)$ measurements to check the ferroelectric properties of BaFeF₄. However, the large leakage current impedes the observation of well-shaped $P(E)$ loops. To avoid the severe leakage problem, we use piezoresponse force microscopy by SPM taken in the normal mode of atomic force microscopy to confirm the ferroelectric properties. Clear butterfly shaped phase-voltage and amplitude-voltage hysteresis loops can be observed, as shown in Fig. 3(c), indicating the ferroelectric properties of BaFeF₄. The nearly 180° phase change indicates the total reverse of ferroelectric polarization might be realized because a much higher electric field can be applied from the acute tip with a very small radius.

The macroscopic magnetism is characterized by measuring the $M(H)$ curves at various temperatures, as shown in Fig. 4(a). It can be clearly seen that S-shaped $M(H)$ curves can be observed up to 300 K, in contrast to the previous reported linear $M(H)$ curves for BaMnF₄, BaNiF₄, and

BaCoF₄ [16,17,37]. However, a small coercivity of 7 Oe is observed for the $M(H)$ curve at 300 K, indicating the soft ferromagnetism in BaFeF₄. With further decreasing temperature to < 60 K, the $M(H)$ curves clearly show the hysteresis loop with significantly large coercivity. To further understand the magnetic properties of BaFeF₄, zero-field-cooled (ZFC) and field-cooled (FC) temperature-dependent magnetization $M(T)$ curves are measured, as shown in Fig. 5(a). For the FC process, a magnetic field of 200 Oe is applied. The FC magnetization increases slightly with decreasing temperature to ~ 125 K. Then a drastic decrease of magnetization can be observed. With further decreasing temperature, a hump can be observed with a peak position at ~ 56 K. Below ~ 20 K, the magnetization increases drastically with decreasing temperature. The ZFC magnetization shows a similar trend with FC magnetization, but a bifurcation can be observed at ~ 170 K between the FC and ZFC $M(T)$ curves. With further decreasing temperature, ZFC magnetization shows the drastic drop at slightly higher temperature than FC magnetization. BaMF₄ has a layered structure, with a puckered sheet in the ac plane. Due to the larger separation between the neighboring layers, the interlayer exchange interaction is weaker than the intralayer exchange interaction. Thus, two-dimensional antiferromagnetism is formed inside each layer first with decreasing temperature [e.g., BaMnF₄ (50 K), BaNiF₄ (150 K), and BaCoF₄ (95 K)] [16,17,37]. With further decreasing temperature, three-dimensional antiferromagnetism is formed. Though the two-dimensional antiferromagnetic transition in BaFeF₄ has not been reported, it is reasonable to attribute the sudden drop of magnetization at ~ 125 K to the form of the two-dimensional magnetic structure. The hump at 56 K, close to the previously reported T_N of ~ 60 K for BaFeF₄, can be attributed to the three-dimensional antiferromagnetic transition [10]. The separation between FC and ZFC $M(T)$ curves starts at 170 K, indicating that the intralayer antiferromagnetic exchange interaction emerges at 170 K. However, in the beginning, only antiferromagnetic clusters formed in the paramagnetic bulk due to the slight inhomogeneous distribution of each element or electronic fluctuation. With further decreasing temperature, the antiferromagnetic clusters expand and finally connect. Then the two-dimensional antiferromagnetic structure is completely formed.

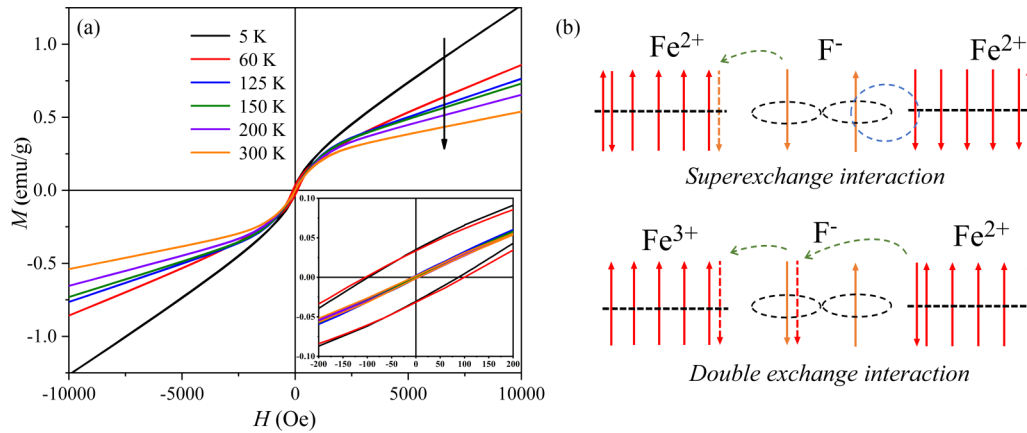


FIG. 4. (a) Magnetic field dependence of magnetization $M(H)$ at different temperature cooled under the magnetic field of 1000 Oe; the inset is the enlarged view. (b) The schematic diagram for the superexchange interaction between Fe^{2+} ions and the double exchange interaction between Fe^{2+} and Fe^{3+} ions.

Interestingly, the magnetization only shows gradual decrease with increasing temperature up to 300 K and, together with the S-shaped $M(H)$ curve at 300 K with coercivity of 7 Oe, indicates the existence of room temperature weak ferromagnetism. In our previous work on $\text{Sr}_3\text{Fe}_2\text{F}_{12}$, $\text{Ba}_5\text{Fe}_3\text{F}_{19-\delta}$, and $\text{Pb}_5\text{Fe}_3\text{F}_{19}$ prepared using the same raw materials and under similar conditions, only linear $M(H)$ curves have been observed at 300 K, excluding the possible ferromagnetic impurities under the detecting limit [29,38,39]. This is abnormal since such ferromagnetism has not been observed at 300 K in bulk BaMnF_4 , BaCoF_4 , and BaNiF_4 [16,17,37]. In stoichiometric BaFeF_4 , Fe should be in the +2 valence state. As can be seen in Fig. 4(b), due to the ionic bonding between Fe^{2+} and F^- ions, the overlapping of electron clouds is quite small, leading to the much weaker exchange interaction and low magnetic ordering temperature. Furthermore, only superexchange interaction between the Fe^{2+} ions can be established, leading to antiferromagnetism in BaFeF_4 . As confirmed by the XPS results of the existence of Fe^{3+} ions, double exchange interaction might be formed between the neighboring Fe^{2+} and Fe^{3+} ions. The outer shell electronic structure of Fe^{2+} is $3d^6$, while that of Fe^{3+} is $3d^5$. An electron in F^- can jump to the neighboring Fe^{3+} with spin down antiparallel to the local d spins due to the half-filled nature of Fe^{3+} . Then an electron with spin down in Fe^{2+} can jump to F^- to occupy the vacancy. This is called double exchange interaction. After this process, the Fe^{3+} ion becomes Fe^{2+} , while Fe^{2+} changes to Fe^{3+} . Thus, the electronic structure before and after are the same, indicating the degenerated states. This will not only lead to ferromagnetic exchange interaction between the neighboring Fe^{3+} and Fe^{2+} ions but also enhance the interaction strength due to the increased electron hopping possibility. Thus, weak ferromagnetism can be established even up to room temperature. However, due to the nonuniform distribution of Fe^{3+} ions, strong ferromagnetic interaction can only be established at the regions with local high concentration of Fe^{3+} ions. The low concentration of Fe^{3+} ions between these regions induces weak exchange interaction, which is easily reversed by the magnetic field, leading to low coercivity and soft ferromagnetism at high temperature.

The ME effect in multiferroics is typically manifested as controlling ferroelectric polarization by a magnetic field or magnetization by an electric field. However, as stated above that the $P(E)$ loop cannot be obtained due to the leakage problem, pyroelectric current measurement is applied to get the information of ferroelectric polarization. An electric field of 2 kV/cm is applied during the cooling process to temperature of 5 K, and the current is collected during the warming process with increasing temperature rate of 4 K/min. As BaFeF_4 is ferroelectric with Curie temperature of 1093 K [40], a continuous increase of I_{py} can be observed with increasing temperature, which has been subtracted as background signal. As can be seen in Fig. 5(b), a sudden increase of I_{py} can be observed at ~ 170 K, with peak position at ~ 150 K. Here, I_{py} decreases to ~ 0 at ~ 125 K. Under temperature < 125 K, no peak of I_{py} can be observed. Thus, in addition to the change of I_{py} with increasing temperature, the observation of a peak for I_{py} indicates an extra polarization change in the temperature range between 125 and 170 K. The polarization change ΔP is calculated by integrating I_{py} with the time, as shown in Fig. 5(c). Here, ΔP starts to emerge at ~ 170 K and saturate at ~ 125 K to $\sim 34 \mu\text{C}/\text{m}^2$. As studied for the magnetic properties, the onset of ΔP at 170 K coincides well with the onset temperature of two-dimensional antiferromagnetism. The end of the polarization at 125 K is quite close to the end of the two-dimensional antiferromagnetic transition. Thus, it is reasonable to attribute ΔP to the two-dimensional antiferromagnetic transition. We further repeat the pyroelectric current measurement under a magnetism of 90 kOe. The peak position slightly shifts to higher temperature, and the peak height becomes smaller, indicating the possible ME effect. The calculated ΔP saturates at a smaller value of $\sim 30 \mu\text{C}/\text{m}^2$. We also perform the measurement of the magnetic field dependence of ME current I_H , but no clear relation can be observed, as shown in Fig. 5(d) [7]. Similar results are observed at 10 and 60 K. This might be due to the antiferromagnetic structure, which cannot be effectively manipulated by the applied magnetic field. To break the antiferromagnetic structure, a much higher magnetic field is needed. To confirm whether ΔP can be reversed by an electric field, we further perform the pyroelectric current measurement after the application of

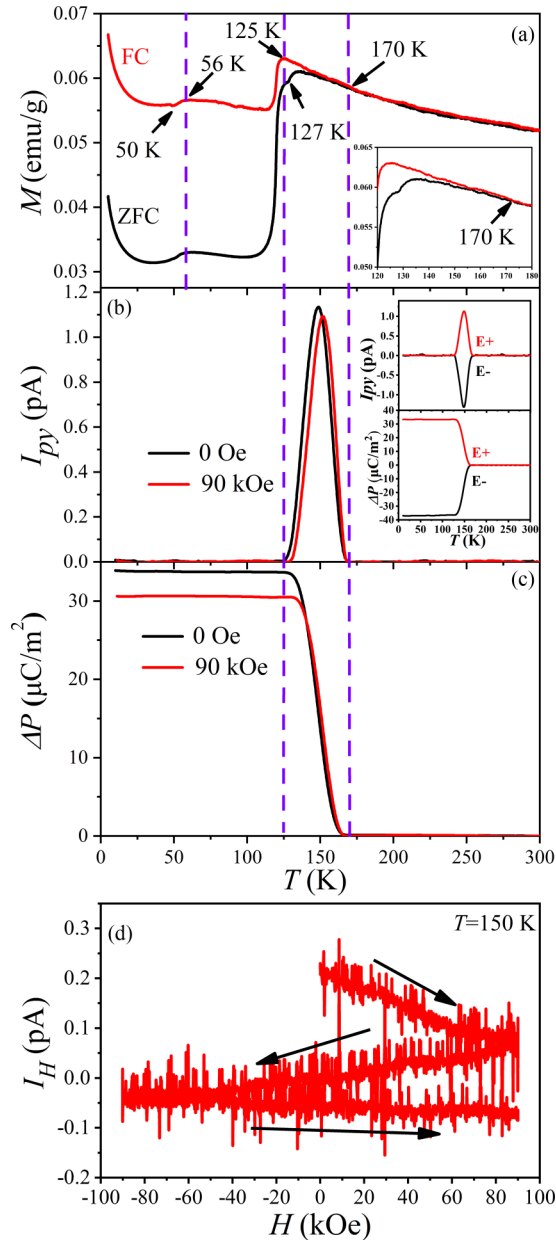


FIG. 5. (a) The field-cooled (FC) and zero-field-cooled (ZFC) magnetization $M(T)$ curves under a magnetic field of 200 Oe; the inset is the enlarged view. (b) The temperature-dependent pyroelectric currents $I_{py}(T)$ curves under different magnetic field. The inset shows the curves of $I_{py}(T)$ and integrated polarization change $\Delta P(T)$ under the positive and negative poling electric field without the magnetic field. (c) The $\Delta P(T)$ curves under different magnetic field. (d) The relationship between the magnetolectric current I_H and the magnetic field H at $T = 150$ K.

an electric field of -2 kV/cm during the cooling process. As shown in the inset of Fig. 5(b), a nearly mirrored $I_{py}(T)$ curve can be observed, and ΔP is reversed by the reversed poling electric field with saturated ΔP of $-36 \mu\text{C}/\text{m}^2$.

C. DFT calculation

To understand the pyroelectric polarization and ME, DFT calculation is performed. With the space group $A2_1am$,

the DFT optimized lattice constants for BaFeF_4 are $a = 5.7252 \text{ \AA}$, $b = 14.9641 \text{ \AA}$, and $c = 4.2622 \text{ \AA}$, which are highly consistent with our experimental results and ensure the accuracy of the following calculation of ferroelectricity. This space group allows a ferroelectric polarization along the a axis. To precisely understand the experimental ΔP , the polarization difference between the antiferromagnetic and paramagnetic states should be accounted. However, the paramagnetic state cannot be treated in standard DFT calculation. A less-than-ideal alternative is using the ferromagnetic state to replace the paramagnetic state, which can qualitatively mimic ME, as done in other pyroelectric systems [41].

Our DFT result of polarization change due to antiferromagnetic transition is $1.704 \mu\text{C}/\text{cm}^2$, qualitatively supporting the experimental ME. The quantitative deviation can be understood as the following. First, our sample is polycrystalline, with randomly oriented crystalline grains, which will reduce the measured polarization for at least one order of magnitude. Second, the grain boundaries in polycrystalline samples will reduce the effective poling voltage. Also, the real ferroelectric transition temperature is far above room temperature; thus, our poling field starting at 300 K is not capable of generating a single ferroelectric domain state with a saturated polarization. Namely, the experimental ΔP should be much smaller than the theoretical saturated value. Therefore, larger ΔP is expectable in further studies with single crystals and higher poling fields. Last, the ferromagnetic state used in the calculation as the baseline is different from the experimental paramagnetic one.

IV. CONCLUSIONS

In summary, polycrystalline multiferroic fluoride BaFeF_4 has been prepared by solid state reaction. The S-shaped $M(H)$ curves is observed at 300 K with coercivity of 7 Oe, indicating the existence of room temperature weak ferromagnetism due to double exchange interaction between the Fe^{2+} and Fe^{3+} ions through the F^- ion. The temperature-dependent pyroelectric current shows a peak at ~ 150 K which starts at 170 K and completes at 125 K. These temperatures coincide well with the onset of two-dimensional antiferromagnetism at 170 K and the end of this magnetic phase transition at ~ 125 K. DFT calculation confirms the polarization change due to the antiferromagnetic phase transition. The ME effect is confirmed by the decrease of saturated ferroelectric polarization change from ~ 34 to $\sim 30 \mu\text{C}/\text{m}^2$ after applying a magnetic field of 90 kOe. The ferroelectric polarization change is also switchable by the reversed poling electric field. The observation of the ME effect with the related mechanism to the magnetic phase transition sheds light on realizing room temperature multiferroic fluorides for practical applications.

ACKNOWLEDGMENTS

This paper is supported by the National Natural Science Foundation of China (Grants No. 51771053, No. 51971109, No. 51802031, and No. 11834002), the Fundamental Research Funds for the Central Universities (Grant No. 2242020k30039), and the open research fund of Key Laboratory of MEMS of Ministry of Education, Southeast University.

- [1] W. Eerenstein, N. D. Mathur, and J. F. Scott, Multiferroic and magnetoelectric materials, *Nature (London)* **442**, 759 (2006).
- [2] S.-W. Cheong and M. Mostovoy, Multiferroics: A magnetic twist for ferroelectricity, *Nat. Mater.* **6**, 13 (2007).
- [3] S. Dong, H. Xiang, and E. Dagotto, Magnetoelectricity in multiferroics: A theoretical perspective, *Natl. Sci. Rev.* **6**, 629 (2019).
- [4] B. B. Van Aken, T. T. M. Palstra, A. Filippetti, and N. A. Spaldin, The origin of ferroelectricity in magnetoelectric YMnO_3 , *Nat. Mater.* **3**, 164 (2004).
- [5] J. Wang, Epitaxial BiFeO_3 multiferroic thin film heterostructures, *Science* **299**, 1719 (2003).
- [6] M. Balli, B. Roberge, P. Fournier, and S. Jandl, Review of the magnetocaloric effect in RMnO_3 and RMn_2O_5 multiferroic crystals, *Crystals* **7**, 44 (2017).
- [7] Y. S. Tang, S. M. Wang, L. Lin, V. Ovidiu Garlea, T. Zou, S. H. Zheng, H.-M. Zhang, J. T. Zhou, Z. L. Luo, Z. B. Yan, S. Dong, T. Charlton, and J.-M. Liu, Magnetic structure and multiferroicity of Sc-substituted hexagonal YbFeO_3 , *Phys. Rev. B* **103**, 174102 (2021).
- [8] N. A. Hill, Why are there so few magnetic ferroelectrics? *J. Phys. Chem. B* **104**, 6694 (2000).
- [9] C. Drathen, T. Nakagawa, W. A. Crichton, A. H. Hill, Y. Ohishi, and S. Margadonna, Structural transition in KMnCrF_6 —a chemically ordered magnetic ferroelectric, *J. Mater. Chem. C* **3**, 4321 (2015).
- [10] M. Eibschütz and H. Guggenheim, Antiferromagnetic-piezoelectric crystals: BaMe_4 ($M = \text{Mn, Fe, Co and Ni}$), *Solid State Commun.* **6**, 737 (1968).
- [11] M. Eibschütz, H. J. Guggenheim, S. H. Wemple, I. Camlibel, and M. DiDomenico, Ferroelectricity in $\text{BaM}^{2+}\text{F}_4$, *Phys. Lett. A* **29**, 409 (1969).
- [12] M. DiDomenico, M. Eibschütz, H. J. Guggenheim, and I. Camlibel, Dielectric behavior of ferroelectric BaMF_4 above room temperature, *Solid State Commun.* **7**, 1119 (1969).
- [13] E. T. Keve, S. C. Abrahams, and J. L. Bernstein, Crystal structure of pyroelectric paramagnetic barium manganese fluoride, BaMnF_4 , *J. Chem. Phys.* **51**, 4928 (1969).
- [14] C. Ederer and N. A. Spaldin, Electric-field-switchable magnets: The case of BaNiF_4 , *Phys. Rev. B* **74**, 020401(R) (2006).
- [15] D. L. Fox and J. F. Scott, Ferroelectrically induced ferromagnetism, *J. Phys. C: Solid State Phys.* **10**, L329 (1977).
- [16] S. Zhou, J. Wang, X. Chang, S. Wang, B. Qian, Z. Han, Q. Xu, J. Du, P. Wang, and S. Dong, Magnetoelectricity coupled exchange bias in BaMnF_4 , *Sci. Rep.* **5**, 18392 (2015).
- [17] S. Zhou, J. Wang, Q. Xu, and J. Du, The wasp-waisted hysteresis loop and exchange bias in multiferroic BaNiF_4 , *AIP Adv.* **7**, 055827 (2017).
- [18] G. Kresse and J. Furthmüller, Efficient iterative schemes for *ab initio* total-energy calculations using a plane-wave basis set, *Phys. Rev. B* **54**, 11169 (1996).
- [19] P. E. Blöchl, Projector augmented-wave method, *Phys. Rev. B* **50**, 17953 (1994).
- [20] J. P. Perdew, A. Ruzsinszky, G. I. Csonka, O. A. Vydrov, G. E. Scuseria, L. A. Constantin, X. Zhou, and K. Burke, Restoring the Density-Gradient Expansion for Exchange in Solids and Surfaces, *Phys. Rev. Lett.* **100**, 136406 (2008).
- [21] C. Ederer and N. A. Spaldin, Origin of ferroelectricity in the multiferroic barium fluorides BaMF_4 : A first principles study, *Phys. Rev. B* **74**, 024102 (2006).
- [22] S. L. Dudarev, G. A. Botton, S. Y. Savrasov, C. J. Humphreys, and A. P. Sutton, Electron-energy-loss spectra and the structural stability of nickel oxide: An LSDA + U study, *Phys. Rev. B* **57**, 1505 (1998).
- [23] R. D. King-Smith and D. Vanderbilt, Theory of polarization of crystalline solids, *Phys. Rev. B* **47**, 1651 (1993).
- [24] R. Resta, Macroscopic polarization in crystalline dielectrics: The geometric phase approach, *Rev. Mod. Phys.* **66**, 899 (1994).
- [25] J. R. Veira, D. N. Argyriou, K. Kiefer, A. U. B. Wolter, D. Alber, M. Meissner, R. Almairac, M. Reehuis, and H. N. Bordallo, Structural and magnetic properties of the ferroelectric magnet $\text{BaMn}_{1-x}\text{Zn}_x\text{F}_4$, a site diluted square-lattice two-dimensional Heisenberg antiferromagnet with $S = \frac{5}{2}$, *Phys. Rev. B* **78**, 054104 (2008).
- [26] Q. Xu, C. Dai, J. Wang, C. Li, Q. Li, and J. Du, Enhanced ferromagnetism in BaNiF_4 film, *J. Alloys Compd.* **741**, 265 (2018).
- [27] B. H. Toby and R. B. Von Dreele, GSAS-II: The genesis of a modern open-source all purpose crystallography software package, *J. Appl. Crystallogr.* **46**, 544 (2013).
- [28] P. Gredin, A. Pierrard, M. Samouel, and A. deKozak, The crystal structure of BaFeF_4 , *C. R. Acad. Sci. B* **323**, 865 (1996).
- [29] F. Zhang, D. Xu, T. Liu, B. Niu, D. Wu, M. Xu, J. Du, and Q. Xu, The magnetic properties of multiferroic $\text{Ba}_5\text{Fe}_3\text{F}_{19-\delta}$, *J. Magn. Magn. Mater.* **541**, 168541 (2022).
- [30] Y. Yu, R. Liu, H. Zhao, Y. Xu, B. Xu, Q. Li, J. Du, and Q. Xu, Room temperature multiferroic BaMnF_4 films, *J. Magn. Magn. Mater.* **494**, 165782 (2020).
- [31] Y. Lu, Z. Wen, J. Jin, X. Wu, and K. Rui, Size-controlled synthesis of hierarchical nanoporous iron based fluorides and their high performances in rechargeable lithium ion batteries, *Chem. Commun.* **50**, 6487 (2014).
- [32] D. D. Hawn and B. M. DeKoven, Deconvolution as a correction for photoelectron inelastic energy losses in the core level XPS spectra of iron oxides, *Surf. Interface Anal.* **10**, 63 (1987).
- [33] A. P. Grosvenor, B. A. Kobe, M. C. Biesinger, and N. S. McIntyre, Investigation of multiplet splitting of Fe 2p XPS spectra and bonding in iron compounds, *Surf. Interface Anal.* **36**, 1564 (2004).
- [34] N. Zhou, L. Gan, R. Yang, F. Wang, L. Li, Y. Chen, D. Li, and T. Zhai, Nonlayered two-dimensional defective semiconductor $\gamma\text{-Ga}_2\text{S}_3$ toward broadband photodetection, *ACS Nano* **13**, 6297 (2019).
- [35] J. Yu, X. Kuang, J. Li, J. Zhong, C. Zeng, L. Cao, Z. Liu, Z. Zeng, Z. Luo, T. He, A. Pan, and Y. Liu, Giant nonlinear optical activity in two-dimensional palladium diselenide, *Nat. Commun.* **12**, 1083 (2021).
- [36] Z. Zeng, X. Sun, D. Zhang, W. Zheng, X. Fan, M. He, T. Xu, L. Sun, X. Wang, and A. Pan, Controlled vapor growth and nonlinear optical applications of large-area 3R phase WS_2 and WSe_2 atomic layers, *Adv. Funct. Mater.* **29**, 1806874 (2019).
- [37] S. Zhou, C. Dai, Q. Xu, and J. Du, The magnetic properties of multiferroic BaCoF_4 , *AIP Adv.* **7**, 055822 (2017).
- [38] Y. H. Yu, W. Mi, Q. Li, J. Du, and Q. Y. Xu, The magnetic properties of multiferroic $\text{Sr}_3\text{Fe}_2\text{F}_{12}$, *J. Magn. Magn. Mater.* **502**, 166516 (2020).
- [39] D. S. Xu, F. Zhang, B. Niu, J. Du, D. Wu, Q. Li, M. X. Xu, and Q. Y. Xu, Magnetic properties of multiferroic $\text{Pb}_5\text{Fe}_3\text{F}_{19}$, *J. Magn. Magn. Mater.* **541**, 168540 (2022).

- [40] J. F. Scott and R. Blinc, Multiferroic magnetoelectric fluorides: Why are there so many magnetic ferroelectrics? *J. Phys.: Condens. Matter* **23**, 113202 (2011).
- [41] Y. Zhang, L. Lin, J.-J. Zhang, X. Huang, M. An, and S. Dong, Exchange striction driven magnetodielectric effect and potential photovoltaic effect in polar CaOFeS, *Phys. Rev. Materials* **1**, 034406 (2017).